Geophysical Journal International

Geophys. J. Int. (2014) **196,** 1441–1454
Advance Access publication 2014 January 9

doi: 10.1093/gji/ggt490

Efficient inversion of three-dimensional finite element models of volcano deformation

M. Charco[1] and P. Galán del Sastre[2]

[1]*Instituto de Geociencias (CSIC, UCM), Facultad de Ciencias Matemáticas, Plaza de Ciencias* 3*, E-*28040 *Madrid, Spain. E-mail: mcharco@iag.csic.es*
[2]*Departamento de Matemática Aplicada a la Edificación, al Medio Ambiente y al Urbanismo, E.T.S. Arquitectura, UPM, Av. Juan de Herrera* 4*, E-*28040 *Madrid, Spain*

Accepted 2013 December 3. Received 2013 November 30; in original form 2013 February 19

SUMMARY

Numerical techniques, as such as finite element method, allow for the inclusion of features, such as topography and/or mechanical heterogeneities, for the interpretation of volcanic deformation. However, models based on these numerical techniques usually are not suitable to be included in non-linear estimations of source parameters based on explorative optimization schemes because they require a calculation of the numerical approach for every evaluation of the misfit function. We present a procedure for finite element (FE) models that can be combined with explorative inversion schemes. The methodology is based on including a body force term representing an infinitesimal source in the model formulation that is responsible for pressure (volume) changes in the medium. This provides significant savings in both the time required for mesh generation and actual computational time of the numerical approach. Furthermore, we develop an inversion algorithm to estimate those parameters that characterize the changes in location and pressure (volume) of deformation sources. Both provide FE inversions in a single step, avoiding remeshing and assembly of the linear system of algebraic equations that define the numerical approach and/or the automatic mesh generation. After providing the theoretical basis for the model, the numerical approach and the algorithm for the inversions, we test the methodology using a synthetic example in a stratovolcano. Our results suggest that the FE inversion methodology can be considered suitable for efficiently save time in quantitative interpretations of volcano deformation.

Key words: Inverse theory; Numerical approximations and analysis; Volcano monitoring.

1 INTRODUCTION

Volcano geodetic monitoring involves the interpretation of observed deformation. Models provide data interpretation and, therefore, the link between the observed deformation and the inaccessible sources of these effects. One of the simplest available models that is widely used for the interpretation of volcano deformation is the Mogi model (Mogi 1958). Retaining most of the computational simplicity of elastic half-space models as Mogi one, other analytical models can include topographic effects that could be significant in volcanic areas (e.g. Williams & Wadge 2000). However, it is well known that the internal structure of a volcano and source geometry control the details of the deformation field. In the case of fully 3-D rheologies as well as complicated geometrical structures, a numerical method, such as finite element method (FEM), is needed to simulate volcano deformation. The widespread availability of geodetic data, the constant improvement of numerical methods and the evolution of even more powerful computers keep pushing the range of applications of numerical modelling required for volcanic monitoring development.

Within the elastic frame, a variety of numerical models have been proposed to account for volcano deformation. Dieterich & Decker (1975) investigate 2-D surface deformation caused by magma reservoirs that have different geometries by using FEM. More recently, FEM-based models take into account heterogeneous configurations (Trasatti *et al.* 2003; Manconi *et al.* (2007, 2010); Masterlark 2007; Magni *et al.* 2008a,b). Furthermore, some works deal with the intention of combining inversion methods with numerical models. Fukushima *et al.* (2005) develop a technique to retrieve complex dyke geometries from geodetic data. This approach is based on a combination of a boundary element method with realistic topographic relief and a neighbourhood algorithm (Sambridge 1999a,b). Trasatti *et al.* (2008, 2009) provide a technique to perform inversions of geodetic data using FEM models. In this case, the forward model is a library of numerical displacement solutions, where each entry of the library is the surface displacement due to a single stress component applied to an element of the mesh. The pre-computed forward models are implemented again in the global search algorithm proposed by Sambridge (1999a,b). Manconi *et al.* (2009) and Pepe *et al.* (2010) combine COMSOL (www.comsol.com) models

with Monte Carlo optimization procedures (simulated annealing and/or genetic algorithm) in order to analyse and interpret ground deformation measured at active volcanic areas. More recently, Masterlark *et al.* (2012) automate the estimation of deformation source parameters using a 3-D FEM scheme to simulate volcano deformation. Their simulations are mesh dependent because the source is included as a boundary in the domain. To solve this problem, they apply the pinned mesh perturbation method (Huebner *et al.* 2001), which imposes geometric perturbations and remeshing to define any changes in the position of the deformation source in explorative optimization schemes.

In this work, we develop a numerical inversion algorithm to estimate the optimal parameters for the location and pressurization of a spherical magma chamber. The key to the methodology lies in the technique used to incorporate the source in order to efficiently use finite element (FE) models in inversion algorithms. Deformation sources are included independently of the simulation mesh by considering that three orthogonal dipoles of suitable amplitude yield the same displacement field outside the source as that of including a purely deviatoric stress field around a mesh cavity where pressure acts when source radius is small enough. This methodology holds one inherent advantage for inverse estimations of the parameters describing the deformation source: it minimizes the computational time in fully automated schemes by preventing remeshing and the assembly of the linear system of algebraic equations that defines the numerical approximation.

The layout of the paper is as follows. The description of the problem, including equations and formulation, is presented in Section 2. Section 3 introduces the numerical procedure for volcano deformation simulation. It is verified against a known analytical solution. Section 4 describes the implementation of an optimization method for solving the inverse problem and finally, in Section 5, we present an application of the methodology to a stratovolcano.

2 PROBLEM STATEMENT: VOLCANO DEFORMATION

Model assumptions are the core of any quantitative interpretation of deformation data through the inversion of a given population of data. Our intention here is to study the response of an elastic media to an internal load that can reflect any tectonic, magmatic and/or hydrothermal processes at depth that results in strain. This classical problem of solid earth geophysics can be formulated mathematically as a boundary value problem. In this section, we briefly cover the formulation of this problem and refer to extensive literature for more details (e.g. Malvern 1969). Attention is focused on how to introduce the internal load into the problem. This provides some clues for solving inverse problems using 3-D FEM models.

2.1 Boundary value problem for elastic deformation

Consider a solid $\Omega \subset \mathbb{R}^3$ with a Lipschitz boundary Γ, the conservation of linear momentum states that:

$$\frac{D}{Dt}\int_\Omega \rho \mathbf{v} = \int_\Gamma \mathbf{T} + \int_\Omega \rho \mathbf{f}, \tag{1}$$

where $\mathbf{T}$ is the traction acting on the boundary Γ, that is related to stress, $\boldsymbol{\sigma}$, via $\mathbf{T} = \boldsymbol{\sigma}.\mathbf{n}$ ($\mathbf{n}$ being the unit outward normal vector), $\rho\mathbf{f}$ are body forces per unit mass (ρ being the density), $\mathbf{v}$ is the instantaneous particle velocity and $\frac{D}{Dt}$ denotes the material time derivative operator. For an arbitrary domain Ω, we limit our study to slow static changes that occur over long time periods and to permanent offsets associated with volcanic events. Furthermore, we take into account the momentum balance and the Reynolds transport theorem. Therefore, the inertia term can be neglected and the mechanical behaviour of earth materials is described by means of:

$$\nabla \cdot \boldsymbol{\sigma} + \rho\mathbf{f} = 0. \tag{2}$$

The mathematical models we discuss represent the Earth as an ideal elastic body that is mechanically isotropic. The constitutive relation for an isotropic, linearly elastic solid has the form (Hooke's law):

$$\sigma_{ij} = \lambda \sum_{k=1}^{3} \varepsilon_{kk}\delta_{ij} + 2\mu\varepsilon_{ij}, \tag{3}$$

where $\boldsymbol{\varepsilon}$ is the strain, that is related with the displacement field by $\boldsymbol{\varepsilon} = \frac{1}{2}(\nabla\mathbf{u} + \nabla^T\mathbf{u})$; δ_{ij} is the Kronecker delta; μ represents the shear modulus, also called the rigidity modulus or the second Lamé coefficient, that relates shear stress to strain providing a material rigidity or stiffness under shear and λ is the first Lamé coefficient.

Although for many purposes it is useful to consider a purely elastic and homogeneous medium, volcano structures involve sequences of deposition and emplacement of various materials which have very different mechanical properties, magma intrusion, crystallization and alteration, fracture and shallow hydrothermal systems. Relaxing the homogeneity assumption, the rheological behaviour of rocks can be described by $\lambda = \lambda(\mathbf{x})$, $\mu = \mu(\mathbf{x})$, $\rho = \rho(\mathbf{x})$, where lateral and depth variations of elastic parameters are considered. Thus, the substitution of the constitutive relation (3) in the equilibrium equation (2) yields the equation of motion in terms of displacement field for an elastic domain with variable (heterogeneous) material properties:

$$\frac{\partial}{\partial x_i}(\lambda\nabla\cdot\mathbf{u}) + \sum_{j=1}^{3}\frac{\partial}{\partial x_j}\left[\mu\left(\frac{\partial u_i}{\partial x_j} + \frac{\partial u_j}{\partial x_i}\right)\right] + \rho f_i = 0, \tag{4}$$

with $i = 1, 2, 3$.

Finally, the complete problem statement requires appropriate boundary conditions for the system of eqs (4). The boundary of the domain Ω is divided into parts Γ_1 and Γ_2 (Fig. 1). The eq. (4) is then followed by the boundary conditions:

$$\left.\begin{array}{ll} \boldsymbol{\sigma}\cdot\mathbf{n} = 0 & \text{on } \Gamma_1 \\ \mathbf{u} = 0 & \text{on } \Gamma_2 \end{array}\right\}, \tag{5}$$

where $\overline{\Gamma_1 \cup \Gamma_2} = \Gamma$, $\Gamma_1 \cap \Gamma_2 = \emptyset$ and are non-empty. The first condition in (5) describes a surface free of loads (free surface), the second corresponds to the fact that, for sufficiently large computational domain, the displacement field is very small on the subterranean boundaries of Ω. These assumptions lead to a well-posed problem.

2.2 Pressurization of the magma chamber: body force term

Generally, the displacement field due to the inflation/deflation of magma reservoirs is considered to be primarily composed of: (i) the effects of an incremental pressure, ΔP; and (ii) the effects produced by the loading of an additional mass. However, Charco *et al.* (2006) showed that the mass contribution is negligible compared to the pressurization contribution in the displacement calculations for spherical sources in elastic-gravitational models that generalize elastic model (4)–(5). Therefore, we assume that surface deformation at active volcanoes is due to pressure changes at depth and we

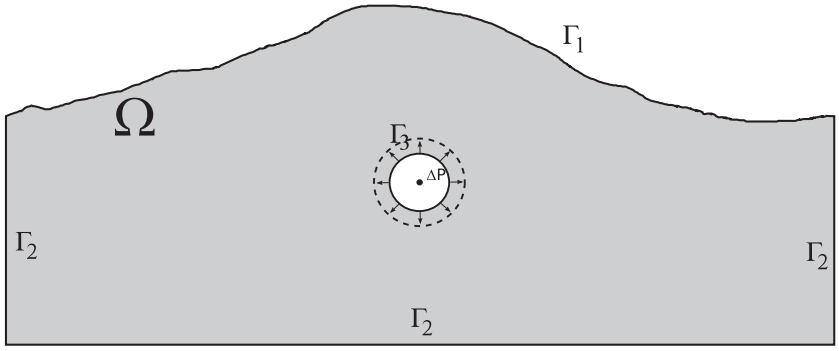

Figure 1. 2-D section of the domain Ω. The pressurization of a magma chamber can be modelled by a spherical cavity inside the medium that expands with uniform pressure ΔP.

focus on spherical reservoirs. In doing so, the inflation/deflation of magma reservoirs is usually modelled by considering a cavity with radius a inside the medium (Fig. 1) where boundary conditions consist of stress boundary conditions appropriate to a uniform change in pressure acting normal to the walls of the cavity. Then, the following boundary condition should be added on the cavity walls, Γ_3, to (5):

$$\boldsymbol{\sigma} \cdot \mathbf{n} = -\Delta P \text{ on } \Gamma_3. \tag{6}$$

When interpreting ground deformation at earth surface, these *a priori* constraints specify, in a unique way, the stress–strain distribution at depth. Nevertheless, the problem domain depends on the cavity location. Thus, solving this problem via FEM implies mesh generation when the source location or geometrical features of the source changes. To gain insight for solving the inverse problem, we consider that the solution for the spherical cavity also can be obtained by assuming three orthogonal force dipoles or centre of dilatation, that is, an isotropically expanding point source (e.g. Mindlin 1936), or three orthogonal tensile dislocations (e.g. Steketee 1958). These conceptually different source models yield the same displacement outside the source, provided an appropriate source strength is designated.

In this work, we consider the body force which would have to be applied in the absence of cavity to produce the same displacement field. Body force representations were used in previous works (e.g. Bonafede & Ferrari 2009; Barbot & Fialko 2010a,b). Here, we assume the source is 'vanishingly small', that is, it is much smaller than its depth. McTigue (1987) showed that the point source approximation holds if the source depth is, at least, three times its radius. In this case, the displacement field due to stress changes in a small spherical cavity are equivalent to the field obtained by the superposition of three mutually orthogonal dipoles of identical strength f_0, that is,

$$\rho \mathbf{f} = f_0 \nabla \delta_{\mathbf{x}=\mathbf{x}'}, \tag{7}$$

where $\delta_{\mathbf{x}=\mathbf{x}'}$ is the Dirac delta distribution that represents a point force (impulse) at $\mathbf{x}'$ (source centre) and the derivatives are equal to a pair of impulses of opposite sign (e.g. Burridge & Knopoff 1964; Aki & Richards 2002). The strength of each dipole is given by Bonafede & Ferrari (2009):

$$f_0 = a^3 \Delta P \frac{\lambda(\mathbf{x}') + 2\mu(\mathbf{x}')}{\mu(\mathbf{x}')}\pi, \tag{8}$$

where the spatial distribution of body forces depends only on the source and the elastic properties of the medium in the immediate vicinity of the source. Because this is an elastic system, the displacement field throughout the domain is a linear function of the source strength, $a^3 \Delta P$. Here, we do not consider the effect of structural discontinuities in f_0 because we are focused on point source solutions and we are not intended to understanding the displacement field near the source. Furthermore, other works devoted to study deformation field by using FEM (e.g. Manconi *et al.* 2007, 2010; Masterlark 2007; Trasatti *et al.* 2008, 2009; Masterlark *et al.* 2012) consider a constant displacement or constant normal stress across cavity walls, neither of which is the most realistic description of medium dilatation.

Since the Dirac delta is the limit of a sequence of Gaussian functions when their variance tends to zero, we define the body force to be applied as:

$$\rho \mathbf{f} = f_0 \frac{1}{\alpha_{x_1}\alpha_{x_2}\alpha_{x_3}\pi^{3/2}} \nabla \left(e^{-\left(\frac{(x_1 - x_1')^2}{\alpha_{x_1}^2} + \frac{(x_2 - x_2')^2}{\alpha_{x_2}^2} + \frac{(x_3 - x_3')^2}{\alpha_{x_3}^2} \right)} \right), \tag{9}$$

where $\alpha_{x_i}^2$ is the variance of the Gaussian function in x_i direction. The size of α_{x_i} is selected *a priori*, depending on the size of the element of the FE discretization. The product $\alpha_{x_1}\alpha_{x_2}\alpha_{x_3}\pi^{\frac{3}{2}}$ is a factor to normalize the Gaussian function per unit volume. As we show in Section 3, this choice ensures that the body force function is sufficiently smooth and suitable to guarantee the solution uniqueness of (4)–(5).

The Gaussian function can be used to model sources of different shapes. When $\alpha_{x_i} = a$ for all $i = 1, 2, 3$, (9) represents a spherical source. However, for $\alpha_{x_1} = a, \alpha_{x_2} = b, \alpha_{x_3} = c$ with $a \neq b \neq c$ and $f_0 = abc\Delta P \frac{\lambda(\mathbf{x}') + 2\mu(\mathbf{x}')}{\mu(\mathbf{x}')}\pi$, (9) can be used to describe an ellipsoidal source with semi-axis a, b and c. Other source geometries can be expressed as weighted combinations of the derivatives of the Gaussian function, taking into account the superposition principle in the elastic case:

$$\rho f_i = \sum_{j=1}^{3} M_{ij} \frac{\partial}{\partial x_j} \left(e^{-\left(\frac{(x_1 - x_1')^2}{\alpha_{x_1}^2} + \frac{(x_2 - x_2')^2}{\alpha_{x_2}^2} + \frac{(x_3 - x_3')^2}{\alpha_{x_3}^2} \right)} \right), \tag{10}$$

where M_{ij} is the moment tensor representing a scaling factor used to model the source as a linear combination of dipoles or double-couples (Eshelby 1957; Aki & Richards 2002).

3 NUMERICAL APPROXIMATION FOR DEFORMATION SIMULATION

This section describes the numerical methodology used to solve the problem. Note that a thorough mathematical treatment of the FE

formulation of the equations is beyond the scope of this study and we refer to the extensive literature for more details (e.g. Brenner & Scott 1994; Ciarlet 2002).

3.1 Weak formulation of the problem

In this work, the authors propose FEM to solve eq. (4) with boundary conditions (5) and a prescribed body force term given by (9). As such, the weak formulation of the problem is required. Let $\mathbf{v} \in C^{\infty}(\Omega)^3$ and suppose that $\mathbf{v}_{|\Gamma_2} = 0$, then, from (4), it is straightforward to prove that

$$\int_{\Omega} \left(\lambda \left(\nabla \cdot \mathbf{u} \right) \cdot \left(\nabla \cdot \mathbf{v} \right) + 2\mu \sum_{i,j=1}^{3} \varepsilon_{ij} \left(\mathbf{u} \right) \varepsilon_{ij} \left(\mathbf{v} \right) \right) = \int_{\Omega} \rho \mathbf{f} \cdot \mathbf{v}, \quad (11)$$

where integration by parts and boundary conditions (5) were applied.

In the following, we use the notation $\mathbf{L^2}(\Omega) = L^2(\Omega)^3$ and $\mathbf{H^1}(\Omega) = H^1(\Omega)^3$. We define the subspace

$$\mathbf{V} = \left\{ \mathbf{v} \in \mathbf{H^1}\left(\Omega\right) : \mathbf{v}_{|\Gamma_2} = 0 \right\}.$$

From (11), we also define the bilinear form $a : \mathbf{V} \times \mathbf{V} \to \mathbb{R}$ and the linear function $L : \mathbf{V} \to \mathbb{R}$:

$$a\left(\mathbf{u}, \mathbf{v}\right) = \int_{\Omega} \left(\lambda \left(\nabla \cdot \mathbf{u} \right) \cdot \left(\nabla \cdot \mathbf{v} \right) + 2\mu \sum_{i,j=1}^{3} \varepsilon_{ij} \left(\mathbf{u} \right) \varepsilon_{ij} \left(\mathbf{v} \right) \right),$$

$$L\left(\mathbf{v}\right) = \int_{\Omega} \rho \mathbf{f} \cdot \mathbf{v},$$

so that, the boundary value problem (4)–(5) can be written as follows: find $\mathbf{u} \in \mathbf{V}$ such that

$$a\left(\mathbf{u}, \mathbf{v}\right) = L\left(\mathbf{v}\right) \quad \forall \mathbf{v} \in \mathbf{V}. \quad (12)$$

It is straightforward to prove that problem (4)–(5) is equivalent to problem (12). Moreover, the following result of existence and uniqueness holds.

Theorem. Assume that $\mathbf{f} \in \mathbf{L^2}(\Omega)$ and $\rho, \lambda, \mu \in L^{\infty}(\Omega)$ and suppose that there exists a constant $\gamma > 0$ such that $\rho - \gamma$, $\lambda - \gamma$ and $\mu - \gamma$ are positive real-valued functions. Then, the variational problem (12) has a unique solution.

Proof. The proof is straightforward using the Lax–Milgram theorem and Korn inequality (Brenner & Scott 1994).

3.2 FEM formulation

Suppose that $\Omega \subset \mathbb{R}^3$ is an open bounded subset with Lipschitz boundary and D_h is a partition of $\bar{\Omega}$ such that $D_h = \{R_j\}_{j=1}^{N_e} \subset \bar{\Omega}$, where R_j denotes a hexahedron and N_e is the number of FEs in the partition. For any j, we define $h_j = \mathrm{diam} R_j$ and $\beta_j = \sup\{\mathrm{diam} S : S \text{ a ball contained in } R_j\}$. As usual, we assume that $\bar{\Omega} = \bigcup_{j=1}^{N_e} R_j$ and the elements R_j satisfy the following regularity conditions: (i) any face of R_j is either a subset of $\partial\Omega$ or any other face of any R_i, with $i \neq j$; (ii) there exists a constant $\alpha > 0$ (that does not depend on the partition D_h) such that $h_j/\beta_j < \alpha$ for all $1 \leq j \leq N_e$.

Let $\hat{R} = [-1, 1]^3 \subset \mathbb{R}^3$ be the reference element, then we define the set of polynomials in $\hat{R}$ of degree$\leq m$, with m an integer, $P_m(\hat{R}) = P_m([-1, 1]) \otimes P_m([-1, 1]) \otimes P_m([-1, 1])$. Thus, $P_m(R_j) = \{\hat{p} \circ T_j^{-1} \in C(R_j) : \hat{p} \in P_m(\hat{R})\}$ where $T_j : \hat{R} \to R_j$ is a continuous bijective transformation.

Then, the FE subspaces V_h and V_{h0} associated to the partition D_h are defined as

$$V_h = \left\{ v_h \in C\left(\bar{\Omega}\right) : v_{h|R_j} \in P_m\left(R_j\right) \text{ for all } 1 \leq j \leq N_e \right\},$$

$$V_{h0} = \left\{ v_h \in V_h : v_{h|\Gamma_2} = 0 \right\},$$

so that $\mathbf{V_h} = V_h \times V_h \times V_h$ and $\mathbf{V_{h0}} = V_{h0} \times V_{h0} \times V_{h0}$.

Thus, the FE solution of (4) with boundary conditions (5) is computed by solving the variational formulation: find $\mathbf{u_h} \in \mathbf{V_{h0}}$ such that

$$a\left(\mathbf{u_h}, \mathbf{v_h}\right) = L\left(\mathbf{v_h}\right) \ \forall \mathbf{v_h} \in \mathbf{V_{h0}}, \quad (13)$$

that can be seen as a discretization of problem (12).

Since $\mathbf{V_{h0}}$ is a finite-dimensional space, we can find a basis that generates this space. In this work, we shall consider the FE space generated with polynomials of degree one, $m = 1$. We can compute a basis for $\mathbf{V_{h0}}$ in the following way. Let $l_0, l_1 \in P_1([-1, 1])$ such that $l_0(-1) = 1 = l_1(1)$ and $l_0(1) = 0 = l_1(-1)$. Let $\hat{\phi}_{rst}(x, y, z) = l_r(x) l_s(y) l_t(z)$, with $r, s, t \in \{0, 1\}$, then $\{\hat{\phi}_{rst}\}_{0 \leq r,s,t \leq 1} \subset P_1(\hat{R})$ is a basis of $P_1(\hat{R})$ and $\{\phi_k^j\}_{1 \leq k \leq 8} \subset P_1(R_j)$ is a basis of $P_1(R_j)$, with $\phi_k^j = \hat{\phi}_{rst} \circ T_j^{-1}$ and $k = 1 + r + 2s + 4t$. Let $N = \dim V_{h0}$ and $\{\varphi_i\}_{i=1}^{N} \subset V_{h0}$ such that for any i and j, $\varphi_{i|R_j} = 0$ or $\varphi_{i|R_j} = \phi_k^j$ for any $1 \leq k \leq 8$. Moreover, we assume that $\varphi_i(x_k) = \delta_{ik}$ with $\{x_k\}_k$ the set of vertices associated to the D_h and δ_{ik} the Kronecker delta. It is straightforward to prove that $\{\varphi_i\}_{i=1}^{N}$ is a basis of V_{h0}. Thus, we shall denote

$$\boldsymbol{\psi}_{\mathbf{i}} = \begin{cases} (\varphi_i, 0, 0), & \text{if } 1 \leq i \leq N \\ (0, \varphi_{i-N}, 0), & \text{if } N < i \leq 2N \\ (0, 0, \varphi_{i-2N}), & \text{if } 2N < i \leq 3N \end{cases}$$

so that $\{\boldsymbol{\psi}_{\mathbf{i}}\}_{i=1}^{3N}$ is a basis of $\mathbf{V_{h0}}$.

Then, problem (13) can be formulated equivalently in the following way: find $\mathbf{u_h} \in \mathbf{V_{h0}}$ such that

$$a\left(\mathbf{u_h}, \boldsymbol{\psi}_{\mathbf{k}}\right) = L\left(\boldsymbol{\psi}_{\mathbf{k}}\right), \quad \forall k = 1, 2, \ldots 3N. \quad (14)$$

We define the stiffness matrix $\mathbf{K} \in M_{3N \times 3N}(\mathbb{R})$ and the real vector $\mathbf{b} \in \mathbb{R}^{3N}$ such that $k_{ij} = a(\boldsymbol{\psi}_{\mathbf{i}}, \boldsymbol{\psi}_{\mathbf{j}})$ and $b_i = L(\boldsymbol{\psi}_{\mathbf{i}})$. Since $\mathbf{u_h} = \sum_{i=1}^{3N} u_i \boldsymbol{\psi}_{\mathbf{i}}$, problem (14) becomes: find $\mathbf{u} = (u_i)_{i=1}^{3N} \in \mathbb{R}^{3N}$ such that $\mathbf{Ku} = \mathbf{b}$. Note that the stiffness matrix $\mathbf{K}$ is symmetric and positive definite since the bilinear form a is symmetric and coercive (Brenner & Scott 1994); thus, the conjugate gradient algorithm can be used to compute the numerical solution.

3.3 Validation

Validation is performed on a problem with a known analytical solution, the problem of a small pressurized spherical cavity (point-source approximation) embedded in an elastic half-space known as the Mogi model after Mogi (1958).

Displacements calculated via analytical formula, as given by Yamakawa (1955), are compared to numerical results found using FEM. Note that the FEM solution is computed in a $200 \times 200 \times 50\,\mathrm{km}^3$ domain that approximates the conditions that the displacement field satisfies on the boundary of the Mogi model, where the displacement field vanish as $|\mathbf{x}| \to \infty$. The displacements are caused by a spherical source of $50\,\mathrm{MPa\,km}^3$ strength located at 4 km depth in a homogeneous medium with a Young modulus 50 GPa and a Poisson ratio of 0.21. These correspond to average values for basalts given by Goodman (1989). The variance of the Gaussian function (9) that represents the centre of dilatation

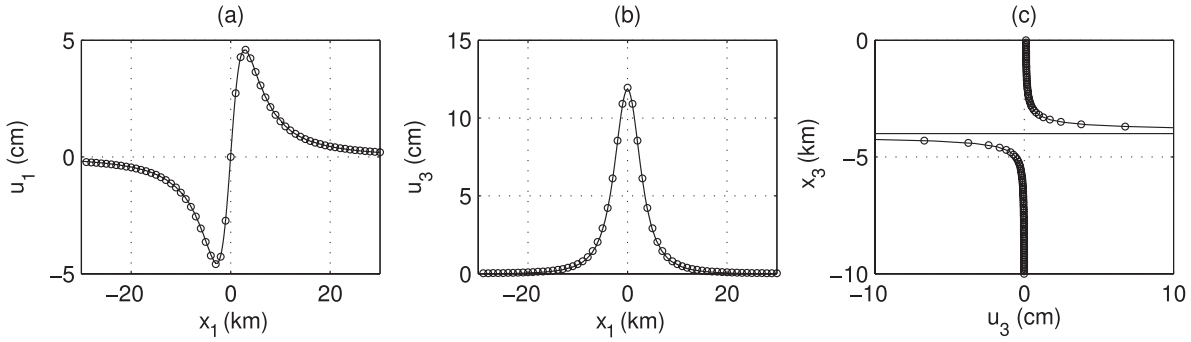

Figure 2. Model comparison of (a) surface horizontal displacements, $u_1(x_1, 0, 0)$, (b) surface vertical displacements, $u_3(x_1, 0, 0)$ and (c) vertical displacements, $u_3(0, 0, x_3)$ between Mogi's analytical solution (circles) and FEM solution (solid line). The displacements are caused by a centre of dilatation of 50 MPa km^3 strength located at 4 km depth in a homogeneous medium.

for FEM solution is chosen according to the mesh element size. In this case, $\sigma_{x_i} = 50$ m for $i = 1, 2, 3$.

Fig. 2 demonstrates that the homogeneous FEM solution agrees with the displacement predicted by Mogi's analytical solution, confirming the reliability of the chosen mesh and boundary conditions. Since the domain for obtaining the solution of the Mogi model is different, we cannot compare both solutions at the exact source location (0, 0, 4) km. In fact, since the source is assumed to be small (point-like in the ideal situation), the deformation of the interior is typically ignored for the Mogi model. Nevertheless, even in the proximity of the source location, there is a good agreement between both solutions (Fig. 2c).

4 INVERSION METHODOLOGY: QUANTITATIVE CHARACTERIZATION OF VOLCANO DEFORMATION SOURCES

Once a deformation model is defined, there are many different techniques to solve the inverse problem. Usually, non-linear formulations require iterative or exploratory processes to reach optimal values that satisfy an objective function, as defined by the model structure, the adopted constraints and the statistical pattern of the parameters (e.g. Aster *et al.* 2005; Tarantola 2005). Hence, the optimization techniques used for volcano deformation interpretation require a balance between robustness and efficiency. In this work, we develop a methodology similar to that proposed by Camacho *et al.* (2007) and Masterlark *et al.* (2012) for estimation of the optimal parameters for the horizontal position, depth and pressurization of a spherical magma chamber based on geodetic data. To efficiently handle non-linear inversions where some of the model parameters are linearly related to the observations, this method combines both a gradient-based technique as least-squares optimization and a sampling strategy.

4.1 Model description: non-linear equations

We estimate the volcanic source parameters performing the inversion of ground deformation measured by a geodetic network that is composed of several stations. The geodetic stations, for example, GPS stations, register changes in the position, that is, the displacement field, caused by subterranean changes in pressure. In the following, we constrain the inversion technique application to spherical sources, given its simplicity, in order to gain important insight into the role of rhelogical properties and topography of the medium. However, the methodology can be extended to different source geometries considering in (4) different source terms of the form (10). We look for the location of the source, $\mathbf{X}' = (x_1', x_2', x_3')$, and the source strength (source volume), $a^3\Delta P$, that involves the pressure change, ΔP. These physical variables are specially important for volcano monitoring and, therefore, for volcanic hazard assessment.

Let $\mathbf{x}_j = (x_{1j}, x_{2j}, x_{3j})$ be the location of the jth station of the network, with $j = 1, 2, \ldots, N$, N being the number of network stations, and let u_{ij} the ith component of the observed displacement field at $\mathbf{x}_j$. To have as much information as possible in order to constrain the source parameters, it would be convenient to measure the three components of the displacement field in all the network stations. Nevertheless, in some cases, horizontal components and the vertical one could have been measured nearly at the same time (i.e. they are related to the same depth processes) but not necessarily at the same stations. Thus, it is possible that at some station, j, the horizontal displacement, u_{1j} or u_{2j}, is observed whereas the vertical component, u_{3j}, is not or vice versa. To properly develop the mathematical framework of the methodology, we define $J_i \subset \mathbb{N}$, $i = 1, 2, 3$, such that $j \in J_i$ if there exist the ith component of the displacement in station j, and $N_i = \text{card}(J_i)$, thus if $j \in J_1 \cap J_2 \cap J_3$, then the full displacement field at station j, $\mathbf{u}_j = (u_{1j}, u_{2j}, u_{3j})$, has been measured.

For a given source location $\mathbf{X}' = (x_1', x_2', x_3')$, let $\mathbf{d} = (u_{ij})_{j\in J_i, i=1,2,3}$ be the $N_1 + N_2 + N_3$ vector of observed geodetic data $\mathbf{u}_j$, then the observed displacements are related to the modelled ones by observation equations of the form:

$$\mathbf{d} = \mathbf{d}^m + \mathbf{v}, \tag{15}$$

where $\mathbf{v} = (v_{ij})_{j\in J_i, i=1,2,3}$, that is, v_{ij} is the residual of the ith component of the displacement at the jth station. This vector contains the residual values coming from observation errors and/or model discrepancies. $\mathbf{d}^m = (u_{ij}^m)_{i=1,2,3,\, j\in J_i}$ is the $N_1 + N_2 + N_3$ vector displacements generated by an incremental pressure, ΔP, at a magma chamber of radius a. In the elastic case, the modelled displacement is proportional to the factor f_0 and, therefore, to the source strength, $a^3\Delta P$. Thus, we can assume that the modelled displacements are a linear combination of contributions from a pressurized magma chamber of strength, $a^3\Delta P$, and some constant terms, u_i^0, that represent, for instance, an unknown position change of the

reference point:

$$u_{1j}^m = g_{1j}\Delta P a^3 + u_1^0,$$
$$u_{2j}^m = g_{2j}\Delta P a^3 + u_2^0, \quad (16)$$
$$u_{3j}^m = g_{3j}\Delta P a^3 + u_3^0,$$

where g_{ij} is the ith component of the displacement field caused by a source of 1 MPa km^3 strength at the station $\mathbf{x}_j$. In doing so, g_{ij} can be understood as a Green's function for the displacement field caused by a pressurized spherical source. Here, the Green's functions are calculated by FEM. Note that the modelled displacement field for the inverse problem computations, $\mathbf{u}_j^m$, is the displacement field (Green's functions) simulated by FEM plus the constant terms described in (16).

4.2 Misfit conditions

In order to find the model parameters, $(x_1', x_2', x_3', \Delta P a^3, u_1^0, u_2^0, u_3^0)$, that explain $N_1 + N_2 + N_3$ observed data, the model system given by (15) and (16) must be fulfilled under some constraints that provide a measure of the discrepancies between observed and modelled data, that is, a measure of $\mathbf{v}$. The misfit or objective function quantifies such differences.

We consider an inverse problem that involves uncorrelated data with Gaussian error distributions and observation equations of the form (15) and (16). An optimal solution can be obtained by minimizing an objective function of the form:

$$\Phi\left(x_1', x_2', x_3', a^3\Delta P, u_1^0, u_2^0, u_3^0\right) = \sum_{i=1}^{3}\sum_{j\in J_i}\frac{v_{ij}^2}{\theta_{ij}^2}, \quad (17)$$

where θ_{ij}^2 are the variances for displacement data values at station j on the x_i direction, as estimated in, for instance, a GPS data adjustment to estimate random observation errors. We are using the l_2-norm to quantify the length of the vector of residuals between observed and modelled position changes. Assuming uncorrelated data, this norm is modified by relative weights that represents a measure of the residuals as function of the data accuracy (observed data variances). The use of the l_2-norm is justified by the application of probability theory: the probability that the observed data are in fact observed is maximum when the quantity given by (17) is minimum, since we are assuming that the data follow a Gaussian distribution and (17) represents $-\frac{1}{2}$ times the argument of the exponential function.

4.3 Numerical implementation

The inversion algorithm minimizes the misfit (17) within predefined model parameters bounds. We observe through system (15)–(16) that our formulation of the inverse problem depends linearly on four parameters, $a^3\Delta P$, u_1^0, u_2^0 and u_3^0, whereas the Green's functions for the displacement field, g_{ij}, depend on source location, $\mathbf{X}'$, in a non-linear way, although this dependency cannot be formally established in the numerical framework. Therefore, the inverse problem for quantitative interpretation of geodetic data constitutes a non-linear optimization problem.

Camacho *et al.* (2007) and Masterlark *et al.* (2012) propose a strategy for solving this kind of problems based on an explorative method by randomly sampling the 3-D parameter space for the source location. After this, they estimate linear parameters in each source location by using least-squares optimization. Therefore, their method requires looking for the displacement field (Green's function) that caused a source located at every possible randomly selected point of the sample space. Here, instead of a random search of source location, we perform a systematic search to show the computational efficiency of the methodology proposed for solving the direct problem (Green's functions computation) using FEM in terms of CPU performance. Random searching of source location involves the repetition of the optimization with different initial random values of $\mathbf{X}'$ in order to ensure a starting point close to the global solution. The systematic search we have implemented ensures such a fact. Furthermore, as it is shown in Fig. 3, the misfit function (17) is, qualitatively, a convex function in our case of study. The systematic search is conducted by uniformly gridding the subsurface volume space inside the source location bounds $x_1' \in (x_{1\min}', x_{1\max}')$, $x_2' \in (x_{2\min}', x_{2\max}')$ and $x_3' \in (x_{3\min}', x_{3\max}')$, where the bounds form a cuboid and are generally given by geological and/or geophysical constraints. The cuboid volume $(x_{1\min}', x_{1\max}') \times (x_{2\min}', x_{2\max}') \times (x_{3\min}', x_{3\max}')$ is then discretized in subcuboids where every subcuboid centre is the potential location of a source centre. Once a source centre has been selected, g_{ij} is computed through FEM and the resulting linear system (15)–(16) must be fulfilled for $\Delta P a^3$, u_1^0, u_2^0 and u_3^0 under the minimization of the objective function (17). This problem constitutes an elementary calculus problem yielding the classical formula for the least-squares optimization. The process is repeated to the whole bunch of subcuboid centres. The objective of this stage is to find an optimal solution that corresponds to the minimum value of the objective function. In doing so, the pressure strength, obtained from least-squares optimization, is substituted in (15) and (16) to determine the value of the objective function (17) corresponding to a particular source realization. Finally, the optimal parameters correspond to the minimum value of the objective function (17).

Next, new explorations are conducted in the neighbourhood of the previous optimal solution to look for a more precise definition of the source location by adaptively decreasing the parameter bounds of $\mathbf{X}'$. In this way, new source location bounds are chosen guided by fitting properties of all previous source realizations. The bounds for the new volume cuboid to be discretized are chosen from the centres of the old subcuboids. We choose this new boundary so that the value of the misfit function is about the same order on it. This self-guided approach concentrates the search around the regions where the subcuboid centres best fit the data and avoids unnecessary areas where the fit is not optimal. Therefore, we incorporate some properties of the misfit function to single out the undetermined source location. The explorative process finishes when either a preset tolerance level is achieved (as a function of the length of the source location bounds) or a default number of direct realizations is reached. The final solution that minimizes the objective function, $\hat{\mathbf{m}} = (\hat{x}_1', \hat{x}_2', \hat{x}_3', \Delta\hat{P}a^3, \hat{u}_1^0, \hat{u}_2^0, \hat{u}_3^0)$, determines the model that best fits the observed data.

Fast and reliable evaluation of deformation sources is very important in early warning and semi-real-time hazard assessment of crustal deformation activities. Nowadays, many computational geophysical problems heavily rely on parallel algorithms to speed up calculations. Such a tendency is continuously growing over time as the available parallel resources increase, in particular with the development of multicore architectures and graphical processing unit computations. The algorithm described above is easy to parallelize since once a source centre is chosen, the direct problem to compute g_{ij} and the resulting least-squares optimization is independent from the rest. Once the least-squares fit and the evaluation of the objective function are performed for every source location, the comparison for finding the minima of (17) is done again in sequential.

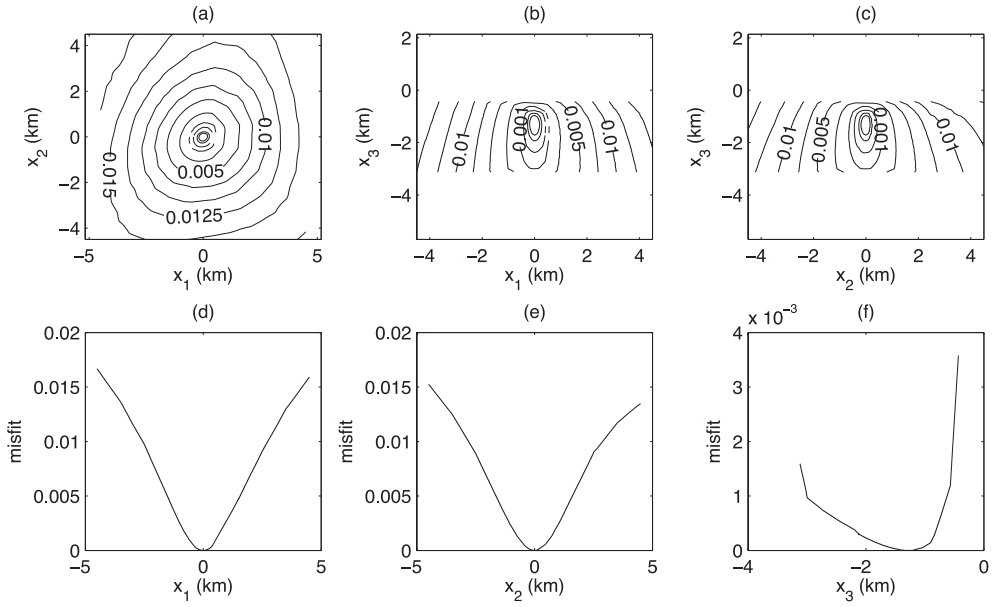

Figure 3. Objective function (17) values. (a) $\Phi(x_1, x_2, -1282)$; (b) $\Phi(x_1, 0, x_3)$; (c) $\Phi(0, x_1, x_3)$; (d) $\Phi(x_1, 0, -1282)$; (e) $\Phi(0, x_2, -1282)$; $\Phi(0, 0, x_3)$.

5 APPLICATION: VALIDATION AND ILLUSTRATION OF THE INVERSION ALGORITHM

The reliability of the model parameters obtained by solving the inverse problem depends, apart from the robustness and efficiency of the inversion technique, on how well model assumptions can approximate the mechanical and rheological properties of the Earth's crust.

Volcanoes, such as Teide volcano (Canary Islands, Spain), are mainly classified as stratovolcanoes based on their internal structure, style and frequency of eruptions. Stratovolcanoes include some of the tallest and best known volcanoes of the world as Fuji in Japan, Vesuvius in Italy, Mayon in Philippines and Teide in Spain. They have steep slopes, particularly in their uppermost parts where slopes may reach 35°–42° (Kilburn & McGuire 2001). The half-space assumption of the Mogi model implies the land surface is flat. On the other hand, a stratovolcano is composed of different types of strata involving the deposition of various materials, lava flows, pyroclastic and sedimentary units and intrusions. Therefore, models of volcano structure should take into account the medium heterogeneities. The deviation from homogeneity is usually simulated by a system of crustal-scale horizontal layers with different elastic properties, that is, by the variation of the elastic properties with depth (e.g. Rundle 1980). We address the implications for misleading assumptions for homogeneity and topography inherent in models, such as the Mogi model, for a stratovolcano as Teide (Tenerife, Canary Islands, Spain). The strategy is to perform and compare some quantitative interpretations, considering different structural models as the core of the inversion scheme. For such a task, first, we calculate the synthetic deformation field caused by an intrusion beneath Teide stratovolcano (Tenerife, Canary Islands, Spain).

5.1 Teide forward model

The eruptive system of Tenerife island is dominated by Teide–Pico Viejo complex which remains active nowadays (e.g. Martí & Geyer 2009). Teide and Pico Viejo are two large stratovolcanoes that overlap to form an elongated double edifice. They are located in the northern part of Las Cañadas Caldera and gave origin to explosive eruptions in the last several thousand years (e.g. Martí *et al.* 2008; Andújar *et al.* 2010). The highest altitude corresponds to the youngest summit of Teide (3718 m).

Fernández *et al.* (2009) and Tizzani *et al.* (2010) provided a summary of previous geodetic studies performed in Tenerife island. GPS and Small Baseline Subset DInSAR analyses show areas of higher subsidence located outside Las Cañadas caldera, as well as a large-scale deformation pattern following the outline of the island that extends beyond caldera rim. While localized areas of subsidence are related to water table variations, the authors proposed that the large-scale deformation pattern is directly related to gravitational sinking of the dense core of the island into a weak lithosphere. In this last case, Tizzani *et al.* (2010) present a 2-D axisymmetric FEM fluid dynamic model to analyse such a process through the evaluation of the viscosity distribution in the medium. Since the geodetic monitoring of the island has not detected any clear anomaly that may be related to volcanic reactivation in Teide–Pico Viejo volcanic system, our model assume that there is a pressure increment of 38 MPa km^3 in a spherical magma reservoir located beneath Teide volcano summit. This allows us to evaluate deformation within and constrained to the caldera rim. Such a pressure increment can represent the injection of magma in a reservoir, volatile saturation of magma or an increase in gas content. Petrological and geochemical studies constrain the magma storage depth at about 5 ± 1 km beneath Teide volcano (Andújar *et al.* 2010), thus we assume the source is located at 5 km depth beneath volcano summit. The evolution state of Teide–Pico Viejo stratovolcanoes has not yet permitted the development of large volumes of magma at such levels (see, e.g. Martí *et al.* 2008), therefore, the point source approximation could be enough to describe the related deformation.

In this application, the complexities taken into account are the topography and mechanical heterogeneities of the island. A system of Cartesian coordinates with the origin located at sea level, just below the Teide summit, is assumed. x_1 and x_2 axes are orientated along the WE and SN directions, respectively, and the x_3 axis points upwards. The 3-D computational domain includes the entire island and its important morphologic features. It is a volume extending 200×200 km^2 in the x_1 and x_2 directions and from 50 km below sea level to the island surface in the x_3 direction. The boundary at the ground surface is taken from a digital elevation model provided by

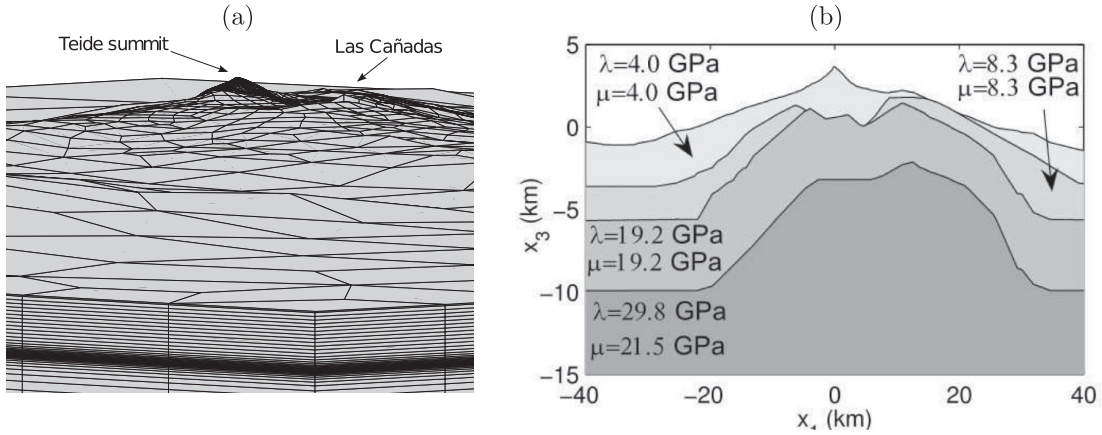

Figure 4. (a) Detailed of the mesh of the computational domain with a spatial resolution of 250 m in the summit area and around the source location and coarse at greater distance; (b) vertical profile at $x_2 = 0$ of the 3-D elastic parameter configuration for Tenerife island.

Instituto Geográfico Nacional (IGN), and a bathymetry model from the 1-min global elevation database (Smith & Sandwell 1997). The computational domain is meshed into 105 094 hexahedron elements and 108 990 nodes (see Fig. 4a). This mesh is locally refined in the vicinity of the chamber and near the Earth's surface. Specifically, the resolution of the mesh is about 250 m in the area where the source is estimated to be located (approximately $10 \times 10 \times 5$ km^3) and a coarse resolution of about 10 km in the rest of the domain. One important aspect concerns the crustal properties. Fig. 4(b) shows a vertical WE profile from the 3-D model of the elastic parameters considered in this study. The elastic parameters were estimated from previous gravimetric and seismic studies carried out in the island (Boshard & MacFarlane 1970; Watts *et al.* 1997; Camacho *et al.* 2011).

Fig. 5 shows the displacement field. Most of the deformation is restricted to the vicinity of Teide volcano and lies inside the Las Cañadas Caldera walls. At distances greater than 5–7 km from the volcano summit, the deformation would be indistinguishable from background noise. The uplift is the largest component of the displacement field, with a maximum value of 10.47 cm at the volcano summit area. The topographic relief of the island and the medium heterogeneities surrounding Teide volcano clearly influence the displacement field. Typical homogeneous half-space solutions for spherical sources create axisymmetrical radial patterns, where the global maximum of vertical displacement resides on the projection of the source on the free surface. In our study case, it coincides with the location of the summit of Teide volcano. We can observe in Fig. 5 that the global maximum of the vertical component deviates from the one that would be obtained using analytical models that assume homogeneous half-space media (e.g. Battaglia & Hill 2009).

To capture the 3-D deformation field caused by the pressure increment, we now consider the geodetic network covering the entire island (Fig. 6). The network is formed by 17 GPS permanent stations. The GPS stations located near Teide volcano are also shown in Fig. 5. All locations approximate, in a reliable way, the real location of the GPS stations installed by the IGN (www.ign.es), Instituto Tecnológico y de Energías Renovables (ITER; www.iter.es) and Cartográfica de Canarias (GRAFCAN; www.grafcan.es). Given the accuracy attainable nowadays by GPS permanent networks, 0.2–0.6 cm and 0.5–1 cm for horizontal and vertical coordinates (Bartel *et al.* 2003), the permanent GPS stations located near Teide volcano could easily measure the displacement field. For example, the vertical displacement in the station located near the volcano summit would reach a value of 10 cm. Since the displacement field depends on pressure change in a linear way, the stations at Teide neighbouring could be able to register a pressure change of around 25 MPa at 5 km depth beneath the volcano summit.

5.2 Inversion results, discussion and concluding remarks

We perform two inversions to estimate the best-fitting sources for the synthetic data that could be observed at the 17 GPS network stations

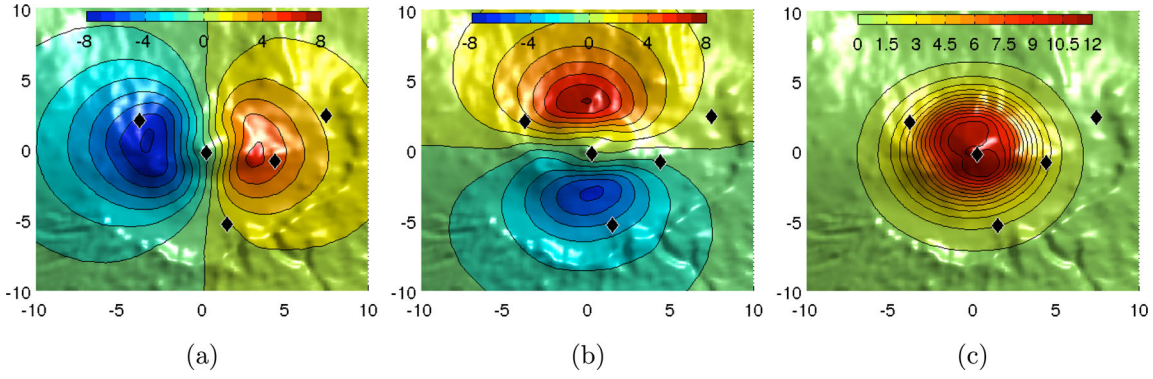

Figure 5. Surface displacement field (cm) caused by a source of 38 MPa km^3 strength located at 5 km depth beneath Teide volcano summit considering both topographic relief of the island and medium heterogeneities: (a) u_{x_1}, (b) u_{x_2} and (c) u_{x_3}. The marks indicate the position of the GPS stations located near Teide volcano.

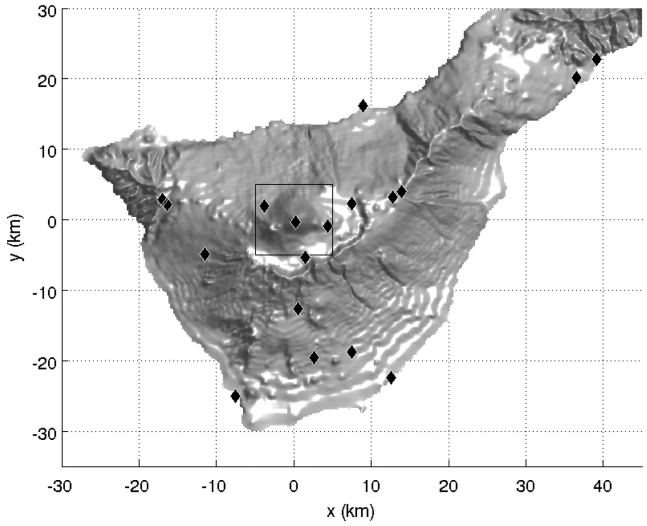

Figure 6. Topography of Tenerife (Canary Islands). The marks indicate the position of the permanent GPS stations located throughout the entire island.

monitoring the island. The synthetic data are provided by the model described above. Since the displacement field vanishes to zero at distances greater than 7 km away from the volcano summit, only stations shown in Fig. 5 provide valuable information for solving the inverse problem.

One inversion is performed considering the Tenerife structural model described in previous subsection, that is, we consider a heterogeneous domain with the actual topography of the island (model TenHeT). This inversion provides reliable information to test the accuracy and robustness of the inversion technique described in Section 4. Therefore, can be used to validate it. The other is performed considering a flat free surface homogeneous domain with the same elastic parameters of the source neighbourhood area in the heterogeneous domain and a reference elevation located at 3000 m above sea level (model TenHoF). Model TenHoF is representative of the analytical models, such as the Mogi model, that are commonly used to investigate quantitative characteristics of magma intrusions in terms of volume (pressure) change and source location. The source centre is restricted to be within a volume of $10 \times 10 \times 3$ km^3 with bounds $x_1' \in (-5000, 5000)$ m, $x_2' \in (-5000, 5000)$ m and $x_3' \in (-3282, -282)$ m. The tolerance level in both inversions is achieved when the length of the source location bounds is less than 50 cm.

Table 1 summarizes the parameters of the best-fitting models. A comparison of their performance is performed through the value of the objective function (17). Thus, we can check that TenHeT performs much better than TenHoF. This synthetic case demonstrates that the model parameters are close to their true values and they are recovered in a very acceptable way (model TenHeT). Then, the inversion technique can be validated.

Table 1. Results of the inversion of the Tenerife synthetic data at the GPS network stations for models TenHeT (heterogeneous medium with topography) and TenHoF (homogeneous medium with flat free surface).

Parameter	True model parameters	TenHeT	TenHoF
S_1 (m)	0	0.0	249.438
S_2 (m)	0	−0.02304	40.1976
S_3 (m)	−1282	−1281.986	−1200.3
$d(\mathbf{S}, \hat{\mathbf{S}})$ (m)		0.027	265.53
$a^3 \Delta P$ (km^3 MPa)	38	37.9998	51.017
u_1^0	0	-1.743035×10^{-8}	−0.0024
u_2^0	0	-8.307691×10^{-8}	3.064×10^{-4}
u_3^0	0	1.773909×10^{-8}	0.0037
Misfit value		$1.5017220 \times 10^{-12}$	0.00132

Fig. 7 shows the source centres location obtained by the optimization process together with the stratification of elastic parameters. This figure and the parameters summarized in Table 1 show that the source position is retrieved by TenHeT with uncertainties as small as the subcuboids size (±50 cm), which proves that the refinement used to solve the inverse problem in the neighbourhood of the source location is acceptable for lateral and depth variations of the elastic parameters. The source strength (Table 1) is determined with an error less than 0.1 per cent when considering the TenHeT model, whereas the error is around 34 per cent when a homogeneous domain with flat free surface (model TenHoF) is considered to perform the inversion. Source strength, $a^3 \Delta P$, depends on both pressure change and source radius and their individual contributions to the magnitude of the displacement field could not be separated. We can use this parameter to estimate an equivalent change in volume of the magma reservoir. The change in volume is directly proportional to source strength (McTigue 1987). Therefore, neglecting topography and medium heterogeneities may lead to overestimating the source volume variation by as much as 30 per cent. The intrusion of fresh magma into a reservoir is thought to be a key component for volcanic eruption triggering. The volume change together with geophysical data, such as spatiotemporal changes in gravity that provide a measure of the density change, is commonly used to estimate mass changes inside the medium (e.g. Rymer 1994). Thus, a bias in this estimation could lead to erroneous interpretations of volcanic unrest that are essential to related monitoring efforts.

Synthetic differences between the observed GPS data and predictions from a model, are usually presented to justify and asses the suitability of a particular deformation model. Accordingly, Fig. 8 shows the differences between the synthetic displacement field and the displacement field retrieved by TenHeT after the inversion, considering the parameters in Table 1. The marks again indicate the stations of the GPS network located in the vicinity of Teide volcano. The differences are on the order of 10^{-4} cm. Considering the GPS precision attainable nowadays, we can conclude that the developed inversion methodology of geodetic deformation data observed at the GPS network of the Tenerife island is very accurate.

Comparison between predictions from TenHeT and TenHoF models reveals sensitivities to TenHoF assumptions. The synthetic displacement field calculated through TenHeT is affected by the elastic properties of the domain area between the source location and the surface. In this application, the upper part of the domain is softer than the lower part, where the source is located in TenHeT model. Topography also affects the synthetic displacement field since the topographic relief increases the distance between source location and the free surface of the domain. In this case, where we show the cumulative effect of the combination of both effects, the source inferred with TenHeT is deeper and smaller (strength/volume) than the one obtained through TenHoF inversion (Table 1). Predicted deformation from TenHeT practically recovers the synthetic deformation field (Figs 8c and f). On the other hand, the quality of the inversion results is unreliable for the TenHoF model since the influence of the medium assumptions produces residuals that are out the range of the observation precision (Fig. 9), approximately 3 cm in both the vertical and horizontal components. The magnitude and pattern of these systematic prediction differences suggest that the

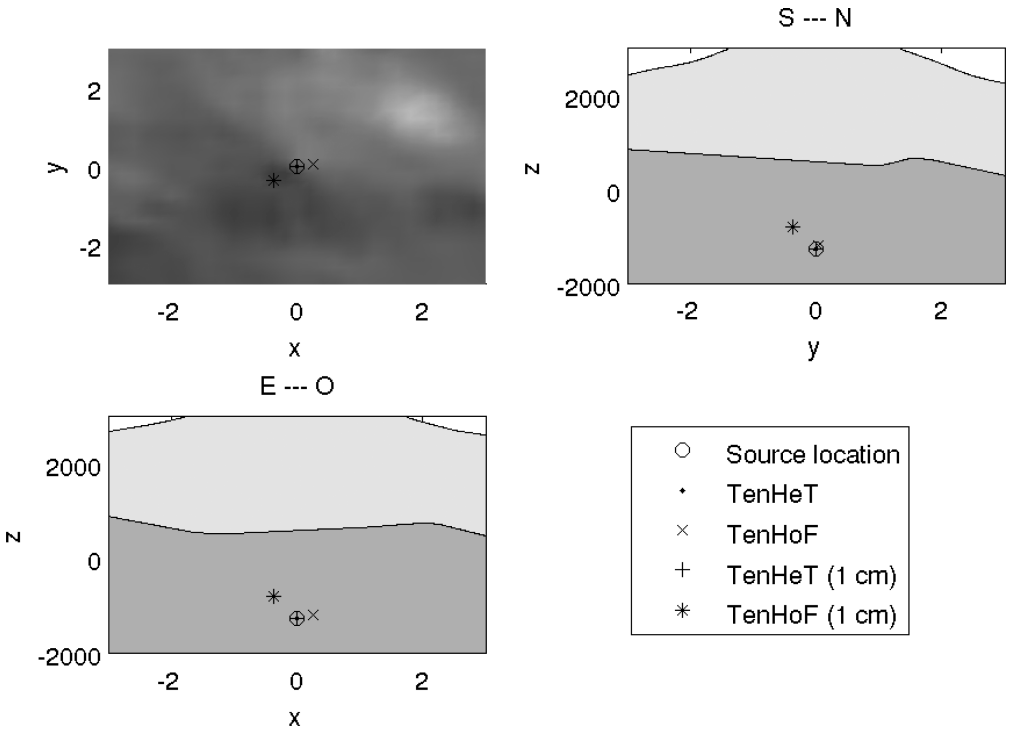

Figure 7. Best-fitting source locations for the inversion of Tenerife synthetic data by using TenHeT and TenHoF. The views are from top, N–S and E–W profiles. The lateral and depth variation of the elastic parameters also is shown in the N–S and E–W profiles.

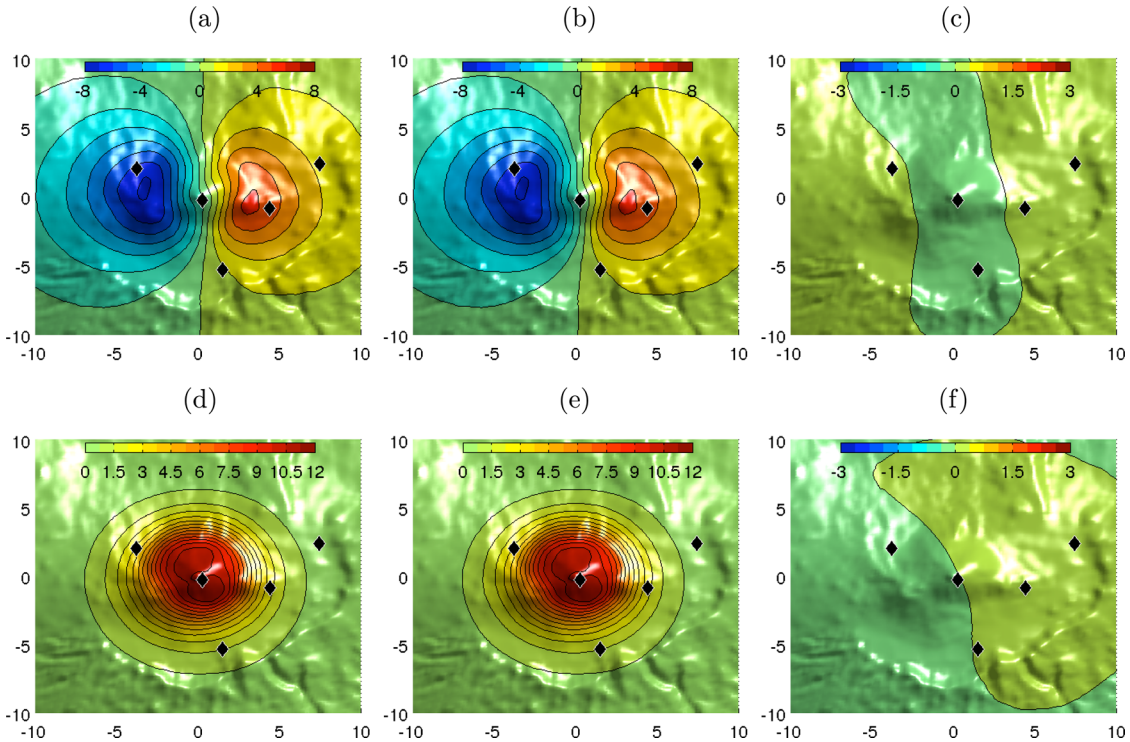

Figure 8. Synthetic components of the displacement field computed by TenHeT (a) u_1 and (d) u_3; (b) u_1^{TenHeT} and (e) u_3^{TenHeT} considering the parameters in Table 1 and resulting from the inversion through TenHeT; forward model residuals: (c) $u_1 - u_1^{\mathrm{TenHeT}}$ and (f) $u_3 - u_3^{\mathrm{TenHeT}}$.

forward model assumptions should be carefully considered when designing a conceptual model of volcano deformation.

In real applications, observations are tainted by different random and systematic errors. We repeat the inversion process, adding a Gaussian noise to the simulated data obtained at the GPS stations. We have included a Gaussian noise with a standard deviation of 1 cm in the three components of the displacement field. It corresponds to about 11 per cent of the non-perturbed vertical signal and 21–49 per cent of the horizontal signal.

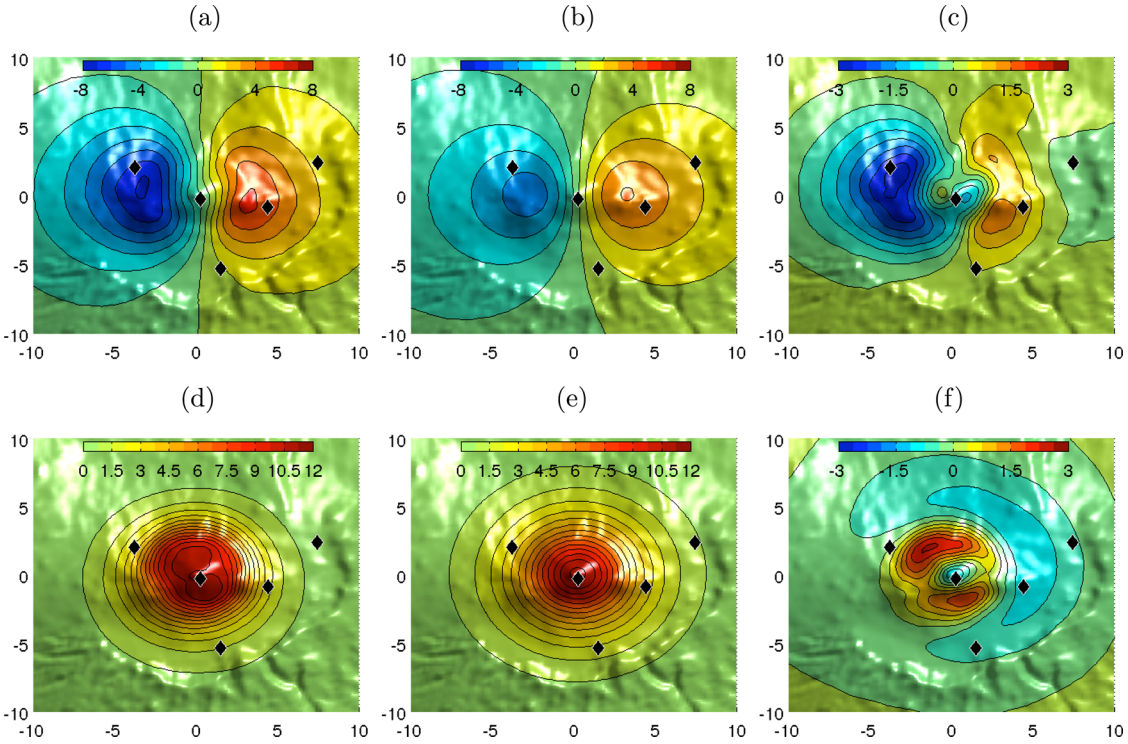

Figure 9. Sensitivities to TenHoF assumptions. Synthetic components of the displacement field computed by TenHeT (a) u_1 and (d) u_3; (b) u_1^{TenHoF} and (e) u_3^{TenHoF} considering the parameters in Table 1 and resulting from the inversion through TenHoF; forward model residuals: (c) $u_1 - u_1^{\text{TenHoF}}$ and (f) $u_3 - u_3^{\text{TenHoF}}$.

Table 2. Results of the inversion of the Tenerife synthetic data at the GPS network stations for models TenHeT (heterogeneous medium with topography) and TenHoF (homogeneous medium with flat free surface). We assume the synthetic data has a Gaussian error of 1 cm.

Parameter	True model parameters	TenHeT (1 cm error)	TenHoF (1 cm error)
S_1 (m)	0	0.0	−364.5
S_2 (m)	0	−0.032	−364.5
S_3 (m)	−1282	−1282.042	−797.85
$d(\mathbf{S}, \hat{\mathbf{S}})$ (m)		0.053	707.22
$a^3\,\Delta P$ (km^3 MPa)	38	38.0035	46.7
u_1^0	0	-4.0087×10^{-8}	−0.0022
u_2^0	0	-2.3838×10^{-8}	-5.1383×10^{-4}
u_3^0	0	-5.2702×10^{-8}	−0.0017
Misfit value		3.10345×10^{-7}	90.078

Table 2 summarizes the parameters of the best-fitting models. As before, it is not difficult to discriminate which model predictions, TenHeT or TenHoF, fit the synthetic values significantly better. Again, Fig. 7 shows the source centres location obtained by the optimization process. The error of the quantitative interpretation provided by TenHoF is aggravated in this case.

Figs 10 and 11 show the differences between the synthetic displacement field and the displacement field calculated by TenHeT and TenHoF with Gaussian error added to the synthetic data. Considering the two examples here, we can conclude that the source parameters are affected by the precision of the observations which is important in assessing the quality of the inversion results when TenHoF is employed in data interpretation. Furthermore, the residuals (Fig. 10) show that the spatial distribution and the number of the stations, in particular, the stations located near Teide volcano, may not be ideal for understanding the deformation field caused by a magma intrusion beneath its summit when a typical model, such as TenHoF, is used for the inversion of geodetic data. Combining GPS with other techniques, such as InSAR, which provides deformation field maps with high spatial resolution, could improve the quality of quantitative geodetic data inversions by typical models.

A fast and reliable evaluation of deformation sources is very important in early warning and near-real-time hazard assessment of crustal deformation activities. As the quality and temporal and spatial resolution of geodetic techniques increase, the implications of a particular conceptual deformation model at the core of an inversion process must be taken into account, as we show above. Masterlark *et al.* (2012) have also proposed a methodology for the estimation of the linear and non-linear parameters of deformation sources in volcanic areas, taking into account structural medium heterogeneities. They focus on the automation of the mesh generation process in response to perturbation of the position of a simulated magma chamber (spherical cavity) within a FEM domain. As it is pointed out in Section 4, the inversion algorithm we propose is easy to parallelize because each separate realization is independent from the rest. To overcome the limitation of remeshing, which involves changing the source location for each realization required by explorative inversion schemes, a body force term described by expression (9) is included in model formulation. This procedure also avoids the assembly of the linear system of equations representing the FEM approach for each iteration, since changes in the matrix depends solely on changes in the domain that remain fixed in the explorative process associated with source location. We take advantage of these properties and the total analysis time for 9000 realizations of the forward model to reach a tolerance of 50 cm (TenHeT model) is about 17 hr. Masterlark *et al.* (2012) employ approximately 7 d on a similar machine (3 GHz quad core CPU) over 12 000 realizations and with an error of over 100 m for source

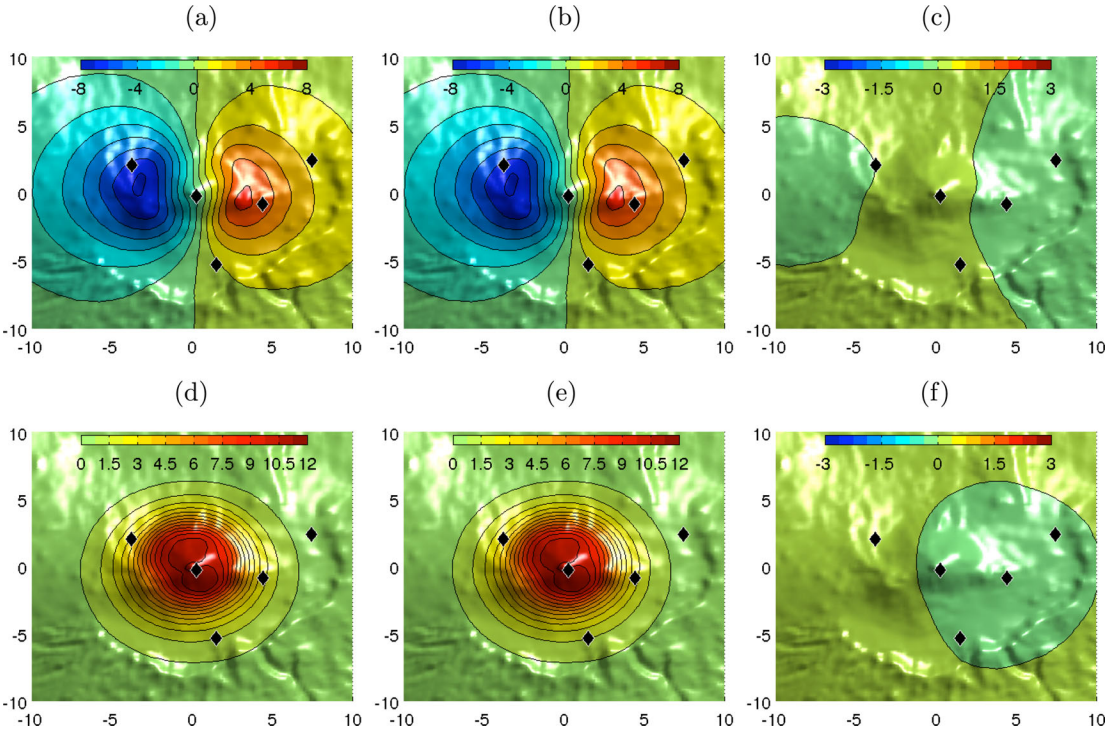

Figure 10. Synthetic components of the displacement field computed by TenHeT (a) u_1 and (d) u_3; (b) u_1^{TenHeT} and (e) u_3^{TenHeT} considering the parameters in Table 2 and Gaussian noise with a standard deviation of 1 cm and resulting from the inversion through TenHeT; forward model residuals: (c) $u_1 - u_1^{\text{TenHeT}}$ and (f) $u_3 - u_3^{\text{TenHeT}}$.

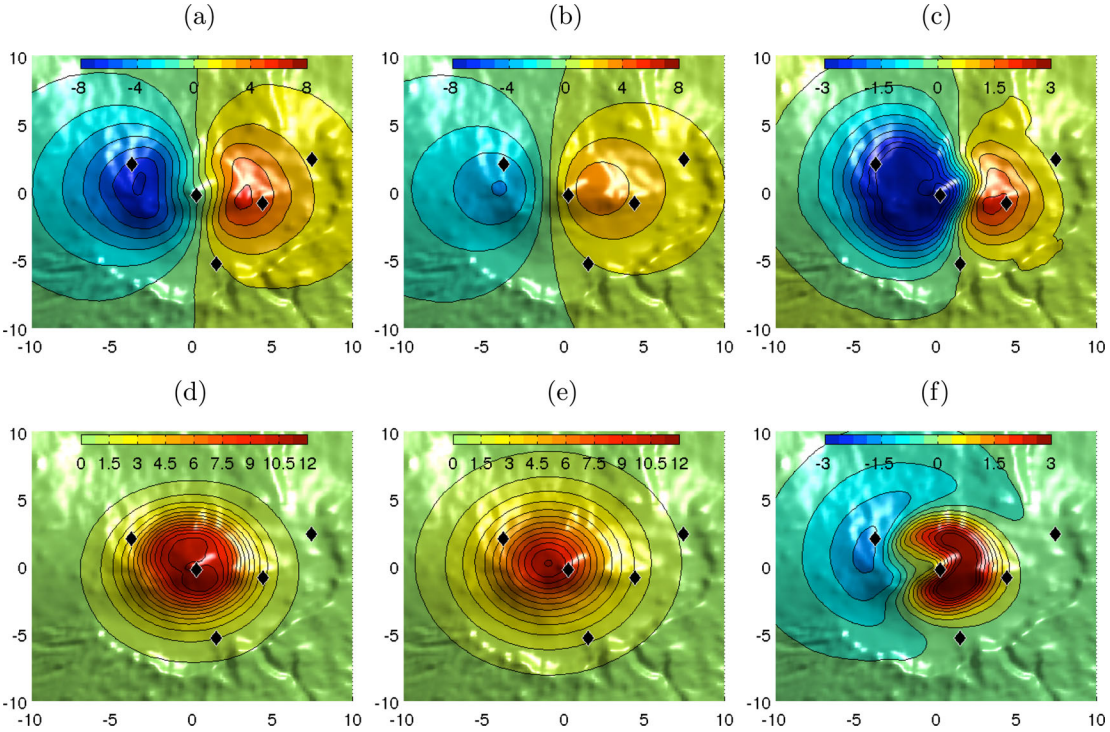

Figure 11. Synthetic components of the displacement field computed by TenHeT (a) u_1 and (d) u_3; (b) u_1^{TenHoF} and (e) u_3^{TenHoF} considering the parameters in Table 2 and Gaussian noise with a standard deviation of 1 cm and resulting from the inversion through TenHoF; forward model residuals: (c) $u_1 - u_1^{\text{TenHoF}}$ and (f) $u_3 - u_3^{\text{TenHoF}}$.

location. Moreover, it is worth mentioning that their mesh contains 13 870 nodes versus the 108 990 nodes that integrates Tenerife mesh. Therefore, the inversion method with heterogeneous models can efficiently be considered in quantitative interpretation of deformation data with significant time savings. Although we describe a suitable and efficient algorithm for FEM inversion, the numerical procedure can be used in other explorative inversion schemes, such as genetic algorithms.

The *a priori* assumption of the source shape could be seen as a limitation of our methodology. However, the procedure for including the source can be extended easily to consider more complex geometries, as briefly described in Section 2. Moreover, although it will be studied in future works, the structural heterogeneities of the medium could be as important as the complex geometry of the source when interpreting displacement field. Further analyses incorporating other kinds of data (InSAR, gravity, etc.) could provide a better understanding of volcanic sources and media.

ACKNOWLEDGEMENTS

The research of MC and PGDS has been support by 200930I053 MICINN-CSIC grant. MC work has also been partially supported by grant CGL2012-37222 from Ministerio de Economía y Competitividad. PGDS work has also been partially funded by grant CGL2007-66440-C04-01 from Ministerio de Educación y Ciencia de España. We would like to thank Kristy Tiampo, Rodolfo Bermejo and Javier Fullea for their suggestions to improve the manuscript. We also thank M. Battaglia, P. Tizzani, C.A. Williams and J. Wasserman for their helpful and valuable comments and suggestions. The numerical codes used in this work are freely available by request to authors.

REFERENCES

Aki, K. & Richards, P.G., 2002. *Quantitative Seismology,* 2nd edn, University Science Books.

Andújar, J., Costa, F. & Martí, J., 2010. Magma storage conditions of the last eruption of Teide volcano (Canary Islands, Spain), *Bull. Volcanol.,* **72**(4), 381–395.

Aster, R.C., Borchers, B. & Thurber, C.H., 2005. *Parameter Estimation and Inverse Problems,* Elsevier Academic Press.

Barbot, S. & Fialko, Y., 2010a. Fourier-domain Green function for an elastic semi-infinite solid under gravity, with applications to earthquake and volcano deformation, *Geophys. J. Int.,* **182**(2), 568–582.

Barbot, S. & Fialko, Y., 2010b. A unified continuum representation of post-seismic relaxation mechanisms: semi-analytic models of afterslip, poroelastic rebound and viscoelastic flow, *Geophys. J. Int.,* **182**(3), 1124–1140.

Bartel, B.A., Hamburguer, M.W., Mertens, C.M., Lowry, A.R. & Corpuz, E., 2003. Dynamics of active magmatic and hydrothermal systems at Taal Volcano, Philippines, from continuous GPS measurements, *J. geophys. Res.,* **108**(10), ECV4-1–ECV4-15.

Battaglia, M. & Hill, P.D., 2009. Analytical modeling of gravity changes and crustal deformation at volcanoes: the Long Valley caldera, California, case study, *Tectonophysics,* **471**(1–2), 45–57.

Bonafede, M. & Ferrari, C., 2009, Analytical models of deformation and residual gravity changes due to a Mogi source in a viscoelastic medium, *Tectonophysics,* **471,** 4–13.

Boshard, E. & MacFarlane, D.J., 1970. Crsutal structure of the western Canary Island from seismic refraction and gravity data, *J. geophys. Res.,* **75,** 4901–4918.

Brenner, S.C. & Scott, R., 1994. *The Mathematical Theory of Finite Element Methods,* Springer-Verlag.

Burridge, R. & Knopoff, L., 1964. Body force equivalents for seismic dislocations, *Bull. seism. Soc. Am.,* **54,** 1875–1888.

Camacho, A.G., Fernández, J., Charco, M., Tiampo, K.F. & Jentzsch, G., 2007. Interpretation of 1992–1994 gravity changes around Mayon volcano, Philippines, using point sources, *Pure appl. Geophys.,* **164,** 733–749.

Camacho, A.G., Fernández, J. & Gottsman, J., 2011. A new gravity inversion method for multiple subhorizontal discontinuity interfaces and shallow basins, *J. geophys. Res.,* **116,** B02413, doi:10.1029/2010JB008023.

Charco, M., Fernández, J., Luzón, F. & Rundle, J.B., 2006. On the relative importance of self-gravitation and elasticity in modeling volcanic ground deformation and gravity changes, *J. geophys. Res.,* **111,** B03404, doi:10.1029/2005JB003754.

Ciarlet, P.G., 2002. *The Finite Element Method for Elliptic Problems,* Classics in Applied Mathematics, Vol. 40, Society for Industrial and Applied Mathematics (SIAM).

Dieterich, J.H. & Decker, R.W., 1975. Finite element modeling of surface deformation associated with volcanism, *J. geophys. Res.,* **80**(29), 4094–4102.

Eshelby, J.D., 1957. The determination of the elastic field of an ellipsoidal inclusion, and related problems, *Proc. R. Soc. A,* **241,** 376–396.

Fernández, J. *et al.*, 2009. Gravity-driven deformation of Tenerife measured by InSAR time series analysis, *Geophys. Res. Lett.,* **36,** L04306, doi:10.1029/2008GL036920.

Fukushima, Y., Cayol, V. & Durand, P., 2005. Finding realistic dike models from the interferometric synthetic aperture radar: the February eruption at Piton de la Fournaise, *J. geophys. Res.,* **110,** doi:10.1029/2004JB003268.

Goodman, R.E., 1989. *Introduction to Rock Mechanics,* Wiley.

Huebner, K.H., Dewhirst, D.L., Smith, D.E. & Byrom, T.G., 2001. *The Finite Element Method for Engineers,* John Wiley and Sons, 720 pp.

Kilburn, C.J. & McGuire, W.J., 2001. *Italian Volcanoes,* Terra Publishing.

Magni, V., Battaglia, M., Tizzani, P., Manconi, A. & Walter, T., 2008a. Axial symmetric crustal deformation model for Long Valley Caldera, California, in *Excerpt from Proceedings of the COMSOL Conference 2008,* Hannover.

Magni, V., Battaglia, M., Walter, T. & Tizzani, P., 2008b. Finite element analysis of crustal deformation at Long Valley Caldera (California), *EOS, Trans., Am. geophys. Un.*, **89**(53), Suppl., Abstract V51D–2062.

Malvern, L.E., 1969. *Introduction to the Mechanics of a Continuous Medium,* Prentice-Hall.

Manconi, A., Walter, T.R. & Amelung, F., 2007. Effects of mechanical layering on volcano deformation, *Geophys. J. Int.,* **170,** 952–958.

Manconi, A., Tizzani, P., Zeni, G., Pepe, S. & Solaro, G., 2009. Simulated annealing and genetic algorithm optimization using COMSOL multiphysics: applications to the analysis of ground deformation in active volcanic areas, in *Excerpt from Proceedings of the COMSOL Conference 2009,* Milan.

Manconi, A., Walter, T.R., Manzo, M., Zeni, G., Tizzani, P., Sansoti, E. & Lanari, R., 2010. On the effects of 3D mechanical heterogeneities at Campi Flegrei caldera, southern Italy, *J. geophys. Res.,* **115,** B08405, doi:10.1029/2009JB007099.

Martí, J. & Geyer, A., 2009. Central vs flank eruptions at Teide-Pico Viejo twin volcanoes (Tenerife, Canary Islands), *J. Volc. Geotherm. Res.,* **181,** 47–60.

Martí, J., Geyer, A., Andújar, J., Teixidó, F. & Costa, F., 2008. Assessing the potential for future explosive activity from Teide-Pico Viejo stratovolcanoes (Tenerife, Canary Islands), *J. Volc. Geotherm. Res.,* **178,** 529–542.

Masterlark, T., 2007. Magma intrusion and deformation predictions: sensitivities to the Mogi assumptions, *J. geophys. Res.,* **112,** B06419, doi:10.1029/2006JB0044860.

Masterlark, T., Feigl, K.L., Haney, M., Stone, J., Thurber, C. & Ronchin, E., 2012. Nonlinear estimation of geometric parameters in FEMs of volcano deformation: integrating tomography models and geodetic data for Okmok volcano, Alaska, *J. geophys. Res.,* **117,** B02407, doi:10.1029/2011JB008811.

McTigue, D.F., 1987. Elastic stress and deformation near a finite spherical magma body: resolution of the point source paradox, *J. geophys. Res.,* **92,** 12 931–12 940.

Mindlin, R.D., 1936. Force at a point in the interior of a semi-infinite solid, *Physics,* **7,** 195–202.

Mogi, K., 1958. Relations of eruptions of various volcanoes and deformation around them, *Bull. Earthq. Res. Inst. Univ. Tokyo,* **36,** 99–134.

Pepe, S., Tizzani, P. & Manconi, A., 2010. Numerical inversion of surface deformation at Long Valley Caldera (California) by using 3D mechanical models, in *Excerpt from the Proceedings of the COMSOL Conference 2010,* Paris.

Rundle, J.B., 1980. Static elastic-gravitational deformation of a layered half space by point couple sources, *J. geophys. Res.,* **85,** 5355–5363.

Rymer, H., 1994. Microgravimetric changes as a precursor to volcanic activity, *J. Volc. Geotherm. Res.,* **61,** 311–328.

Sambridge, M., 1999a. Geophysical inversion with a neighborhood algorithm. Part I. Searching a parameter space, *Geophys. J. Int.,* **138,** 479–494.

Sambridge, M., 1999b. Geophysical inversion with a neighborhood algorithm. Part II. Appraising the ensemble, *Geophys. J. Int.,* **138,** 727–746.

Smith, W.H.F. & Sandwell, D.T., 1997. Global seafloor topography from satellite altimetry and ship depth soundings, *Science,* **277,** 1956–1962.

Steketee, J.A., 1958. On Volterra's dislocations in a semi-infinite elastic medium, *Can. J. Phys.,* **36,** 192–205.

Tarantola, A., 2005. *Inverse Problem Theory and Methods for Model Parameter Estimation,* Society for Industrial and Applied Mathematics.

Tizzani, P., Manconi, A., Zeni, G., Pepe, A., Manzo, M., Camacho, A. & Fernández, J., 2010. Long-term versus short–term deformation processes at Tenerife (Canary Islands), *J. geophys. Res.,* **115,** B12412, doi:10.1029/2010JB007735.

Trasatti, E., Cianetti, S., Giunchi, C., Bonafede, M., Piana Agostinetti, N., Casu, F. & Manzo, M., 2009. Bayesian source inference of the 1993–1997 deformation at Mount Etna (Italy) by numerical solutions, *Geophys. J. Int.,* **177,** 806–814.

Trasatti, E., Giunchi, C. & Bonafede, M., 2003. Effects of topography and rheological layering on ground deformation in volcanic regions, *J. Volc. Geotherm. Res.,* **122,** 89–110.

Trasatti, E., Giunchi, C. & Piana Agostinetti, N., 2008. Numerical inversion of deformation caused by pressure sources: application to Mount Etna, Italy, *Geophys. J. Int.,* **172,** 873–884.

Watts, A.B., Peire, C., Collier, J., Dalwood, R., Canales, J.P. & Henstock, T.J., 1997. A seismic study of lithospheric flexure in the vicinity of Tenerife, Canary Islands, *Eath planet. Sci. Lett.,* **146**(3–4), 431–447.

Williams, C.A. & Wadge, G., 2000. An accurate and efficient method for including the effects of topography in three-dimensional elastic models of ground deformation with applications to radar interferometry, *J. geophys. Res.,* **105**(B4), 8103–8120.

Yamakawa, N., 1955. On the strain produced in a semi-infinite elastic solid by an interior source of stress, *J. Seismol. Soc. Japan,* **8,** 84–98.